TEM investigation of SCC crack tips in high Si stainless steel tapered specimens

TEM investigation of SCC crack tips in high Si stainless steel tapered specimens

A. Penders[1,2], M. J. Konstantinović[1], W. Van Renterghem[1], R.W. Bosch[1], and D. Schryvers[2]

[1] SCK CEN, Boeretang 200, 2400 Mol Belgium
apenders@sckcen.be
https://www.sckcen.be/
[2] University of Antwerp, Groenenborgerlaan 171, 2020 Antwerp, Belgium
Electron Microscopy for Materials Science - EMAT
https://www.uantwerpen.be/en/research-groups/emat/

Abstract: The stress corrosion cracking mechanism is investigated in high Si duplex stainless steel in simulated PWR environment based on TEM analysis of FIB-extracted SCC crack tips. The microstructural investigation in the near vicinity of SCC crack tips illustrates a strain-rate dependency in stress corrosion cracking mechanisms. Detailed analysis of the crack tip morphology, that includes crack tip oxidation and surrounding deformation field, indicates the existence of an interplay between corrosion- and deformation-driven failure as a function of the strain-rate. Slow strain-rate crack tips exhibit a narrow cleavage failure which can be linked to the film-induced failure mechanism, while rounded shaped crack tips for faster strain-rates could be related to the strain-induced failure. As a result, two nominal strain-rate dependent failure regimes dominated either by corrosion or deformation driven cracking mechanisms can be distinguished.

Keywords: Stress corrosion cracking, Stainless steel, PWR, TEM, FIB, Film-induced cleavage

1   Introduction

Despite the increasing collection of experimental data and the numerous models proposed in the literature, stress corrosion cracking (SCC) continues to puzzle the scientific community due to the complexity of the underlying physical mechanisms [1–5]. Concerning nuclear power plant (NPP) internals, SCC occurs due to the interplay of several material degradation phenomena that include factors such as stress, water chemistry, temperature and material composition alterations. SCC component failures are observed for example in cold-worked austenitic stainless steel used in NPPs, including incidents related to irradiation-assisted SCC (IASCC) [6–11].

Several studies have been devoted to SCC crack initiation and propagation, with a focus on the evaluation and prediction of time-to-failure ranges. A very common methodology is based on constant load tests in which the material is placed under relevant stress-corrosion conditions and the time-to-failure is measured [12]. Such tests clearly demonstrate that by lowering the applied external stress, the time-to-failure increases. It is argued that under a so-called critical stress limit or stress threshold, the time-to-failure ought to be infinite. Similar conclusions have been obtained by an accelerated test method, in which a single test of a tapered shaped specimen with variable cross-section has been used to identify the stress threshold [13–19]. However, large uncertainties in the observed time-to-failure and critical stresses somewhat restrict the application of this methodology for the determination of the true stress threshold.

Recently, detailed statistical analyses in tapered specimens were performed in order to evaluate the stress threshold for SCC crack initiation and the possible influence of the crack count error towards the threshold uncertainty [19]. Crack density distributions were obtained by developing an advanced crack detection algorithm on iteratively

displaced scanning electron microscopy (SEM) images featuring stress corrosion cracks along the specimen's external gauge length. Supported by means of finite-element analysis, precise crack count densities indicated the existence of an intrinsic scatter related to the crack initiation process, which suggests that stress corrosion cracking is independent of the strain-rate for strain-rates lower than 1.00E−6 s^{-1}. Thus far, two separate failure regimes have been identified: a regime where corrosion processes dominate at low strain-rates, and one where mechanical failure prevails at high strain-rates of about 1.00E-6 s^{-1}. The present study further investigates the stress corrosion cracking mechanism using transmission electron microscopy (TEM) of focused ion beam (FIB) extracted SCC crack tips. The aim is to distinct the local microstructural features of SCC dominated regions at low versus high strain-rates. Characterization techniques such as conventional bright-field/dark field TEM imaging and analytical energy dispersive X-ray spectroscopy (EDS), are able to provide constructive evidence towards the understanding of the leading SCC mechanisms in a series of strained duplex stainless steel specimens. Microstructural analyses performed in this research include the investigation of the crack morphology, plastic deformation and passivation layer analyses in close proximity of the SCC crack tips. The results of this study support the conclusions presented in our previous publication [19].

2   Experimental Methods

2.1   Material

The tapered specimens were fabricated from a tailor made high Si stainless steel alloy within the framework of the Euratom-funded FP6 PERFECT project [20], and previously investigated for SCC initiation and through constant elongation rate tensile (CERT) testing [13,19]. The model alloy has been designed to simulate grain boundary composition indicative to irradiated stainless steels, reflecting the radiation induced Si and Ni segregation at the grain boundaries, under non-irradiated test conditions. The outcome of the Si addition is that the fundamental microstructure develops into a duplex matrix wherein elongated austenite phases are embedded into a ferrite matrix. The material composition can be found in Tab. 1.

Despite the fact that non-irradiated stainless steels are hardly susceptible to SCC [21], this model alloy has been shown to be sensitive to SCC in high-temperature water. Whereas the SCC cracking morphology of irradiated stainless steel is mainly dominated by intergranular fractures, non-irradiated stainless steels show both transgranular and intergranular cracking [21]. Indeed, it was previously shown that the preferred crack growth path under the applied strain-rate conditions is transgranular SCC [19]. Possibly, the Si distribution is more homogeneous throughout the matrix under unirradiated conditions. As such, the cracking mechanism is not necessarily similar as in the case of irradiated conditions. Despite the differences, high Si stainless steel can be considered as a useful surrogate material for simulating SCC in unirradiated conditions as the material is susceptible to SCC in high temperature water without being irradiated [13,19].

Tab. 1: Elemental composition of duplex high Si stainless steel tapered specimens.

	Fe	Cr	Ni	Si	Mn	Cu	Al	C	P	S
Comp (wt. %)	Bal.	19.7	9.98	4.85	1.08	0.22	0.033	0.029	0.008	0.005

2.2 CERT testing

CERT straining was performed through the use of a loading unit in an autoclave set-up under simulated pressurized water reactor (PWR) conditions (2 ppm Li, 1000 ppm B, 30 cm^3 standard temperature pressure (STP) H_2/kg equivalent to 2.66 ppm H_2) at 340 °C temperature. The specimens were first subjected to an initial loading phase in order to set the prerequisite conditions for SCC initiation and to allow for a stable oxide film to grow. After one week of pre-oxidation, the subsequent loading phase was initiated at the corresponding strain-rate. Various strain-rates were applied to a series of high-Si flat tapered tensile specimens, as illustrated in Tab. 2. Strain-rates between 10^{-6} and 10^{-8} s^{-1} were selected in order to cover a representative range in terms of time-to-failures so that the crack initiation may be investigated in view of the surrounding microstructure and sample exposure time. Since the local strain-rate is a function of the varying tapered cross-sectional width, the gauge length bears a strain-gradient during testing which is maximal near the smallest cross-section. The term nominal strain-rate, i.e. the ratio between the tapered gauge length and the displacement rate, is hence introduced as an estimate of the true straining process. Further details of the CERT test set-up can be found in our previous publication [19].

Tab. 2: CERT loading conditions for high-Si stainless steel tapered specimens tested in ambient simulated PWR environments at 340 °C.

Sample No.	Environment	Nominal $\dot{\varepsilon}$ (s^{-1})	F$_{max}$ (N)	Time-to-failure (days)	No. Produced TEM-Lamellae
1	PWR	5.00 E-8	3122	26.57	16
2	PWR	1.00E-7	2909	19.72	10
3	PWR	5.00 E-7	3161	13.53	-
4	PWR	1.00 E-6	2903	11.85	6
5	PWR	5.00 E-6	3153	8.27	14

2.3 FIB analysis

2.3.1 TEM-lamellae preparation

Fully developed SCC crack tips embedded in TEM-lamellae were readily extracted from a series of CERT-tested tapered specimens with the use of a ThermoFisher Scientific Scios DualBeam FIB-SEM. The lamellae were prepared in cross-sectional orientation to the tapered specimen gauge length, i.e. along the crack propagation direction. In this manner, one section of an SCC crack tip is preserved after final thinning. The micromanipulator attached to the injector needle allowed for an in-situ lift-out and transfer of TEM-lamellae to copper support grids where they can be carefully thinned to electron-transparency levels. Tab. 2 illustrates the number of lamellae that were produced for each respective strain-rate. Depending on the local crack density, it was possible to extract a multitude of SCC crack tips simultaneously by adjusting the length of the lamella (averaging 1-2 for regions of low crack density, 5-10 for regions of high density). Striking differences in terms of the applied strain-rate primarily amounted to the variation in crack tip

morphology, oxidation thickness, and surrounding deformation field. FIB extraction of fast-strained tips proved to be significantly more challenging as the tapered surface was typically more deformed, inclined and oxidized. However, regardless of the local surface crack density, crack opening widths/lengths, crack orientation, and location of the cracks along the gauge length, all cracks under investigation remained similar for each respective strain-rate in terms of crack morphology, depth, and surrounding microstructure. To this end, the provided results yield a representative SCC description under the given experimental conditions.

The procedure for SCC crack extraction is described in the supplementary information, and is much in line with what has been previously described in plan-view orientation [22]. Fig. 1 displays the general steps towards SCC crack tip FIB-extraction, following the standard lift-out and thinning procedures. SCC cracks were extracted from the specimen gauge surface in a region of 1 mm close to the main fracture surface where the highest crack density occurred [19], see Figs. 1A-C. During the standard thinning at Fig. 1D, numerous ion milling steps over a range of tilt angles where the ion current was repeatedly reduced, ensured an appropriate lamella thinning in order to attain an electron transparent TEM specimen. The ion voltage and current took values between the range of 30 kV and 1 nA down to 8 kV and 0.25 nA, respectively. At the final low energy cleaning operations, the operating voltages and currents were below 5 kV and 0.048 nA. The cleaning steps were required for the purpose of removing any Ga^+ ion implantation embedded within the remaining specimen volume.
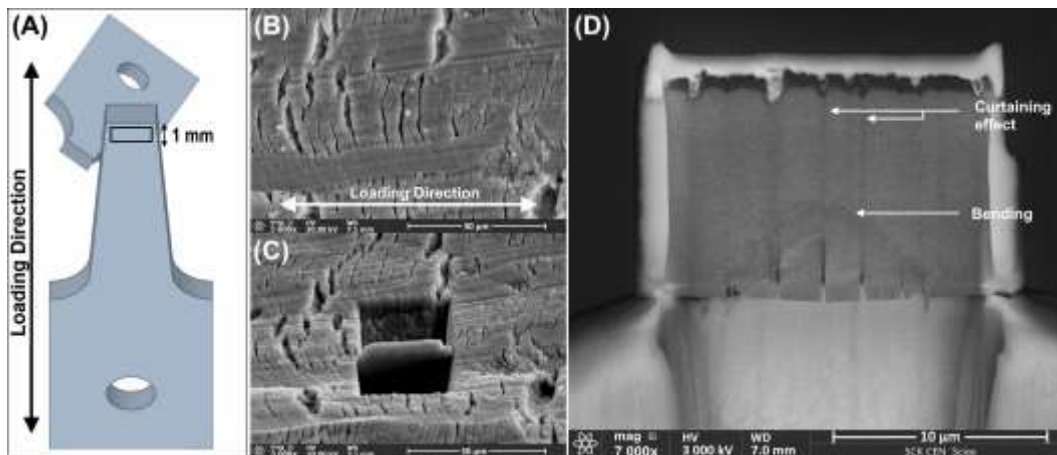

Fig. 1: Visualization of the FIB analysis procedure in the preparation of TEM-lamellae containing SCC crack tips. A: Illustration of the tapered specimen gauge length. The specimen fractures along its smallest cross-section whereon the highest stresses occur. SCC cracks are extracted in close proximity from the main fracture surface. B: SEM imaged fractured surface of a specimen strained to 5.00 E-8 s^{-1}. C: Smoothened trenches on either side of the platinum deposit layer. D: Backscattered electron image after the lift-out procedure and final thinning of a cross-sectional lamella placed on a copper TEM support grid. FIB thinning artifacts like curtaining and lamella bending may arise as the lamella reaches electron-transparency levels.

Incontrovertibly, a curtaining artifact may arise underneath several crack tips, see Fig. 1F. The curtaining may originate due to reasonable changes in the ion-milling rate from an irregular lamella topography, crystal orientation and/or material composition change [23,24]. This typically develops directly beneath each corresponding crack tip and proliferates down to the bottom side of the lamella. The strong channeling effect below each respective crack tip may affect the local lamella thickness and can cause problems like amorphization of the nearby lattice structure. Though,

while this limitation is acknowledged, the latter was generally not observed under TEM. The curtaining effect remains an inherent problem during FIB thinning of SCC cracks that can only be minimized with careful sample preparation. Taking this into account, it was ensured that the morphology of all crack tips under investigation within this research remained visibly unaltered during sample preparation. Hence, it is expected that any drawn conclusions are not affected by the crack curtaining.

2.4 TEM Characterization

Conventional and analytical TEM analyses of FIB-prepared SCC crack tip lamellae were carried out using a 300 kV JEOL 3010 scanning (S)TEM equipped with a LaB_6 electron gun and an Oxford Instrument EDS Link spectrometer with a corresponding Si(Li) detector. Bright- (BF) and centralized dark-field (DF) imaging were used in order to reveal the metallic and oxide phase structures surrounding the SCC crack tips. Centralized DF-TEM imaging is particularly useful when performed using oxide reflections in close proximity of the SCC crack tips. Accordingly, the extent of metal-oxidation is revealed from which the passivation layer thickness may be determined.

Different features surrounding the crack tips were identified using both chemical and diffraction methods. EDS spot-analyses were utilized in order to yield the local chemical composition of the metal to metal-oxide phases in the vicinity of the crack tips. Convergent electron beams impinge upon the sample with the smallest selected spot size, which is estimated to be about 25 nm. Selected area electron diffraction (SAED) oxide patterns may contain ring-like diffraction contributions from many nanocrystalline oxide crystals. The ring intensity profile was rotationally integrated and normalized, thus generating a signal that is unique for the characterization of various oxide phases. The interplanar distance ratios from the experimental diffraction pattern are compared to simulated powder diffraction data in order to present the most probable structure from a known list of candidate structures in the literature.

3 Results and discussion

3.1 FIB analysis

Backscattered electron imaging at low voltages is performed to visualize the grain contrast by utilizing FEI's OptiTilt function as shown in Fig. 2. Grain contrast images of cross-sectional lamellae demonstrate the shallow transgranular cracking nature of SCC in duplex stainless steel. This is in accordance with what has previously been reported under lateral SEM investigation [19]. The deformed grains are elongated in shape and no more than a few square microns in size. Clear contrast variation along the lamella cross-sections unveils the subsequent platinum protection layer, oxide and bulk metal layers. The oxidation film varies slightly in thickness along the gauge length and appears darker under SEM due to the lower backscattered electron count production.
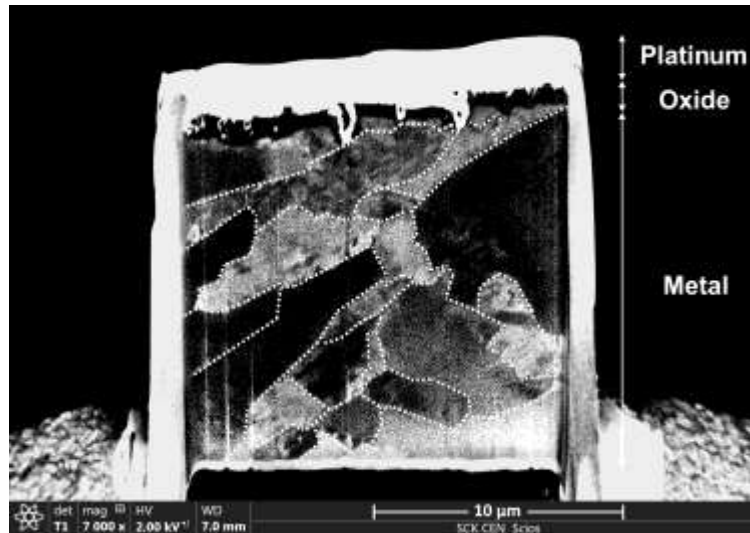
Fig. 2: Low voltage backscattered electron grain contrast imaging of a TEM-lamella containing SCC cracks illustrating the various elongated duplex grains. The dashed lines illustrate the surrounding grain structure of the lamella.

3.2 TEM investigation

3.2.1 Lamella imaging

Conventional TEM of SCC cracks embedded in cross-sectional lamellae orientation is performed in BF-imaging mode from low-indexed zone axes. Low magnification micrographs of the entire lamella can be seen for slow ($\dot{\epsilon}$ = 5.00 E-8 s^{-1}) and fast ($\dot{\epsilon}$ = 5.00 E-6 s^{-1}) strain-rates, respectively in Figs. 3A and 3B. BF-TEM imaged cracks reveal a sequencing of platinum, various oxide and metal layers, and transgranular cracks that either propagate shortly into the bulk metal or arrest within the oxide. Deformation bands are observed as indicators for increased strain concentration in the near vicinity of the crack tips. Furthermore, various twin-slip systems extending deep ahead of the crack tips are distinctly observed for faster strain-rate lamellae. Artefacts stemming from the FIB thinning, such as the occurrence of bend contours and curtaining, cause contrast variation as the lamella is respectively buckled or locally thinner near the crack tip.
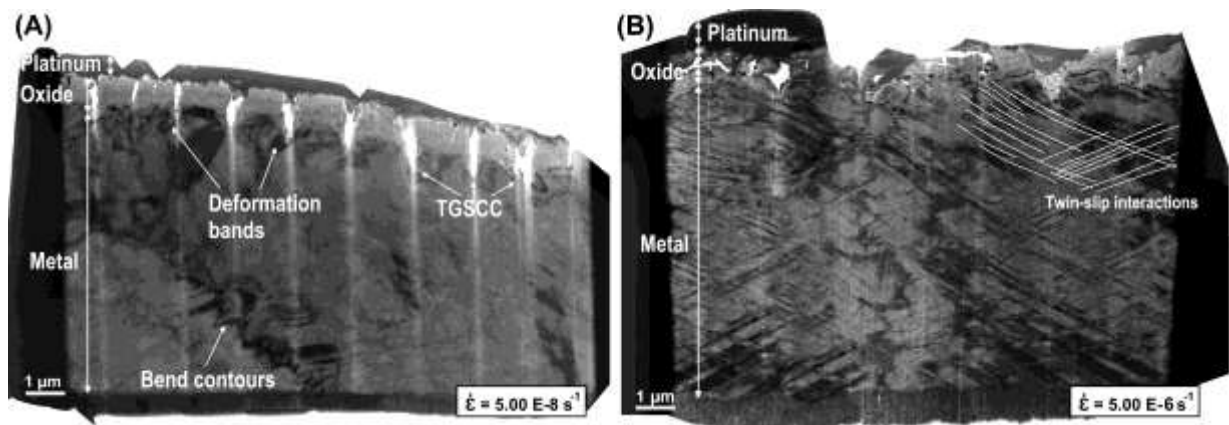

Fig. 3: Low magnification TEM-BF mosaic image composition of the lamella cross-sections of strained tapered specimens with respective strain-rates of, A: $\dot{\epsilon}$ = 5.00 E-8 s^{-1} (slow), and B: $\dot{\epsilon}$ = 5.00 E-6 s^{-1} (fast).

3.2.2 SCC crack tips

Two types of crack tip morphologies depending on the applied nominal strain-rate were commonly observed. Slower strained specimens, $\dot{\varepsilon}$ = 5.00 E-8 s^{-1} and $\dot{\varepsilon}$ = 5.00 E-7 s^{-1}, entailed oxidized cleavage mode SCC cracks which partially propagated into the bulk material before the final arrest, see Fig. 4A. Reasonably long and narrow crack openings were common features at slow-strain-rates. The SCC tips are completely oxidized and arrested in the metal substrate. On the other hand, blunted shaped oxidized crack tips with wide cleavage opening modes were observed for fast-strained specimens at $\dot{\varepsilon}$ = 1.00 E-6 s^{-1} and beyond, see Fig. 4B. SCC cracks extracted from fast-strained specimens routinely blunted within the surface oxide layers near the metal interface or arrested further in the surrounding bulk metal in high tensile stressed regions. Fast-strained crack tips are characterized by an increased roundness and a much wider opening mode of the crack tip. Consequently, the crack tip is typically covered by platinum deposition stemming from the FIB sample preparation. In support of this, the different morphologies are distinguished based on the crack length to width ratio, as shown in Fig. 5. It was found that this ratio steadily decreased with an increasing strain-rate, implying that the crack roundness increased under increased tensile deformation.
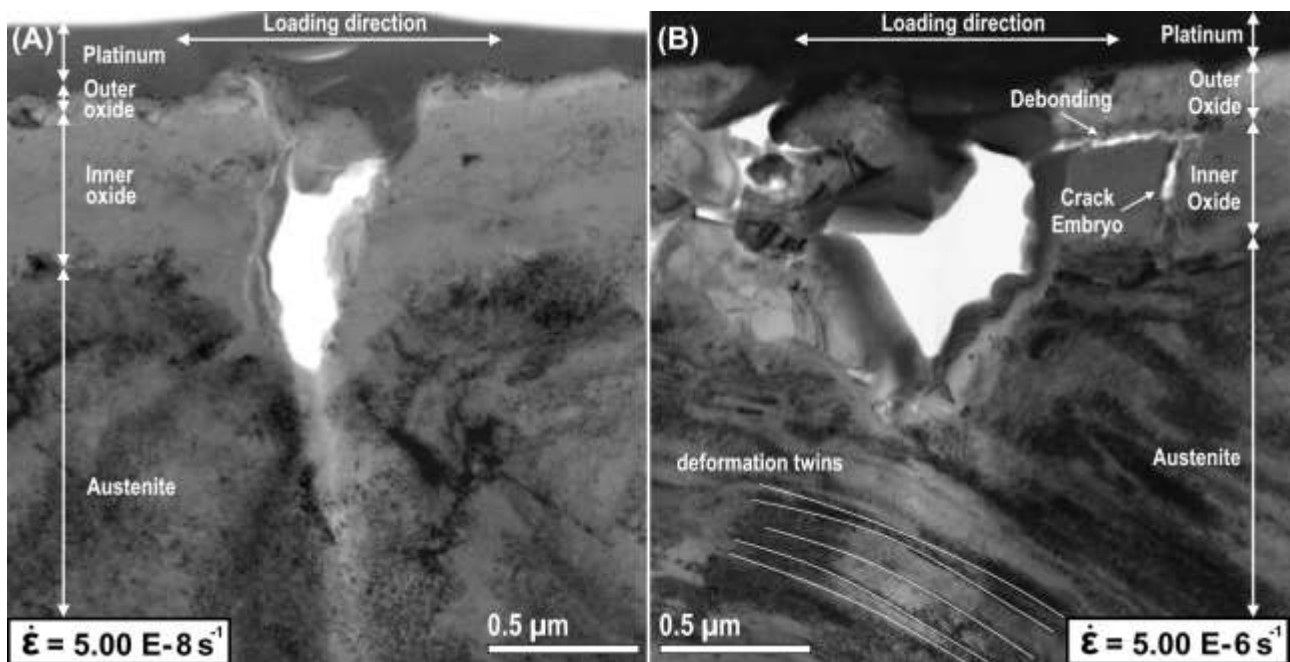

Fig. 4:   Cross-sectional crack morphologies of SCC cracks appertaining to A: $\dot{\varepsilon}$ = 5.00 E-8 s^{-1}, and B: $\dot{\varepsilon}$ = 5.00 E-6 s^{-1}. An increased roundness of the crack tip can be observed in the case of increased nominal strain-rate.

Irrespective of the loading conditions, one can also observe small crack embryo's that initiate at the surface underneath the outer oxide layer. Such cracks generally follow a ragged path and may be filled with outer oxide deposit due to the corrosion processes that take place. The irregular shape suggests that these cracks are the result of brittle oxide fracturing under the applied stress conditions. This is featured by the debonding of the oxide interface which is especially highlighted at high strain-rates as shown in Fig. 4B.
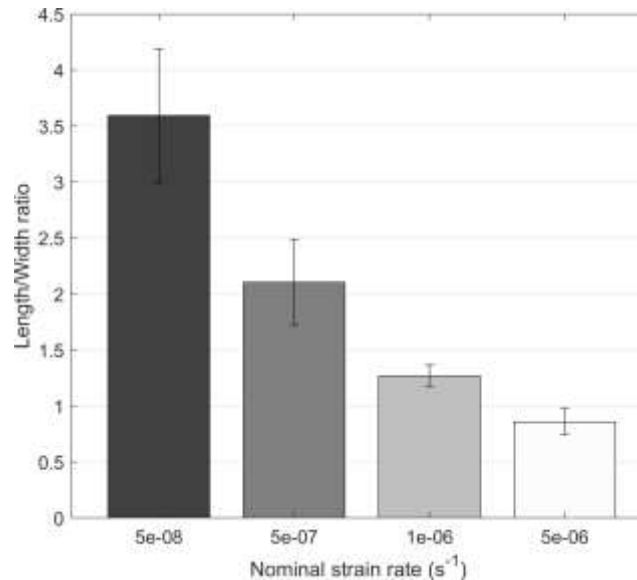
Fig. 5: Comparison of the SCC crack length-width ratio as an indicator for the crack morphology variation in terms of the applied nominal strain-rate. The morphology of the crack tip becomes more rounded with increasing strain-rate.

Fig. 6 displays the case of a microcleavage event under slow strain-rate conditions that propagated for a short distance, in parallel to the crack growth direction, in the inherent inner oxide layer at the pre-existing crack tip. The occurrence of microcleavage events is experimental evidence that the crack initiates within the nucleated inner oxide layer, and that the outer surface oxidation precedes the next crack penetration. In this manner, the crack tip resembles a short-range crack injection which is characteristic to the film-induced cleavage (FIC) model [25, 26]. Indeed, its morphology is a clear example of a transgranular microcleavage injection shown in previously published illustrative diagrams of the FIC model [27]. In order for the crack to grow progressively with each cleavage injection, the film-induced cleavage model proposes that the crack blunts into the bulk material ahead of the pre-oxidized crack. Consecutive surface oxidation nucleation around the blunted crack tip is what is shown in Fig. 6B-C. In the postulated FIC mechanism, small cleavage fractures may initiate in a thin surface film whenever the crack velocity exceeds the oxide repassivation rate. These tips are reasoned to be related to a more developed crack front under influence of strong tensile stresses. In order for the crack to grow progressively with each cleavage injection, the FIC model proposes that the crack blunts into the bulk material ahead of the pre-oxidized crack. Consecutive surface oxidation nucleation around the blunted crack tip is what is shown in Fig. 6B-C. The critical aspects of the FIC model are the strong bonding of a brittle oxide film on the one hand, and the de-alloying in the nanoporous region of crack initiation (in the range of 200 Å) on the other hand [26]. Crack growth in the surrounding metal substrate is a consequence of small cleavage injections which are subjugated to the initial crack entry velocity. Depending on the initial crack length, these crack injections may extend in the range of tens to hundreds of nm, which is supported by our findings.
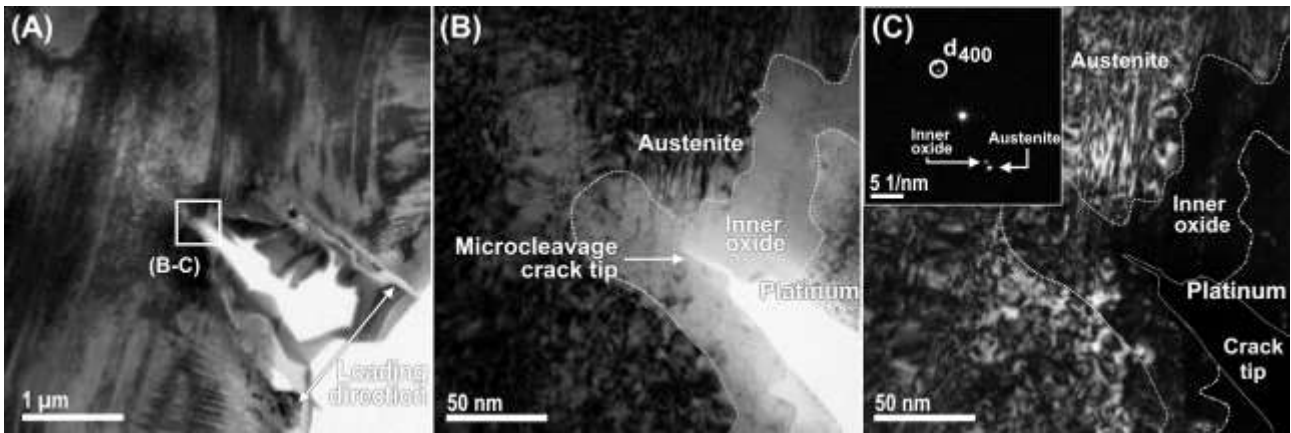
Fig. 6: Two-beam micrographs of an embedded microcleavage crack tip for a lamella belonging to a specimen slowly strained to $\acute{\epsilon}$ = 5.00 E-7 s-1. A: BF-TEM overview, B-C: Respective BF- and centralized DF-TEM of the magnified crack tip. The metal and oxide reciprocal reflections are indexed in the inset diffraction pattern, and the experimental objective aperture is illustrated with the small circle. The reciprocal lattice spacing between both diffraction spots is small, therefore one cannot easily distinguish between the two phases.

It appears that the dissimilar cracking morphology, based on the strain-rates, suggests that a different cracking mechanism takes place for slow and fast strain-rates. Primarily, with concern to the plastic deformation field in front of the respective crack tips, it becomes clear that mechanical twinning becomes more activated under increased levels of externally applied load. At slow strain-rates, plastic strain is typically concentrated in the form of deformation bands near the grain-boundaries and around the SCC crack tips. This typically illustrates the plastic zone in the bulk metal where the highest stresses occurred. However, for fast strain-rates, the intensity of mechanical twinning becomes much more apparent, as seen in Fig. 7. The indexing of the diffraction pattern illustrates that the common twinning plane is along the $(11\bar{1})$ plane. Twin-slip interactions have been commonly observed, especially in the vicinity of crack tips appertaining to fast-strained specimens. At intermediate strain-rates, a balance between these two strain-rate extremes in terms of plastic deformation was noted.
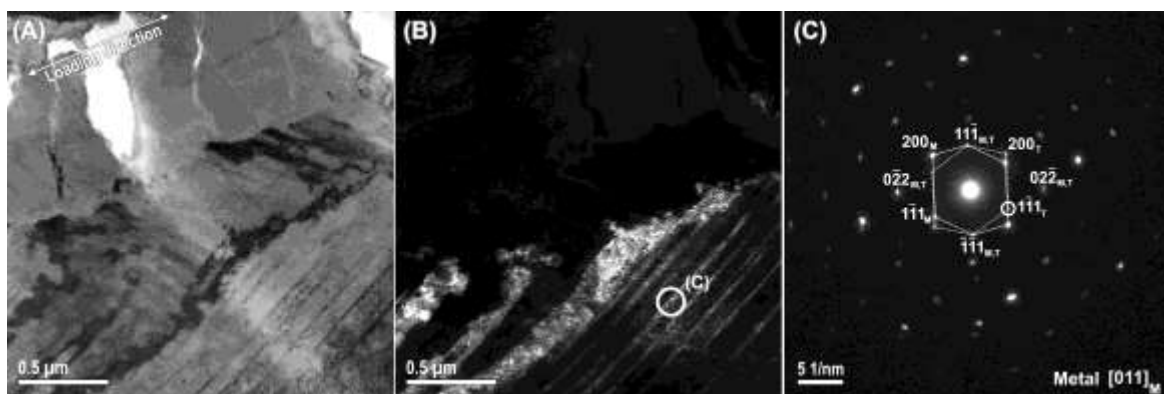

Fig. 7: Twinning microstructure of the deformed metal matrix for a specimen appertaining to the sample strained to $\acute{\epsilon}$ = 5.00 E-6 s^{-1}. A: BF-TEM, B: centralized DF-TEM, and C: the corresponding SAED diffraction pattern of twin structures. The objective aperture used in B is shown by the small circle. The structural model of the matrix (M) and twin (T) indexing illustrates that twinning predominantly occurs along the {111} directions.

3.2.3   Crack tip oxidation

With respect to the external and crack tip oxidation films, a double layered oxide was confirmed using both diffraction and EDS point analyses. The outer oxide typically consists of large crystallites, whereas the inner oxide exclusively consists of randomly oriented nanocrystallites, see Fig. 8. The BF and centralized DF images clearly illustrate the extent of oxidation in front of the crack tip and along the external gauge surface. Correspondingly, the oxidation film thicknesses are measured and presented in Fig. 9. A significant trend regarding a change in crack tip oxidation in terms of the applied strain-rate was not observed. The apparent increment at high strain-rates is still below the precision of the measurement making the trend difficult to verify. In contrast to slow-strained specimens, fast-strained specimens are typically more oxidized at the external surface due to an increase of the outer oxide thickness. Moreover, an increasing trend of outer oxidation at the expense of the inner oxide can be observed. This is in agreement with previous studies which have shown that external stresses can have an increasing effect of the surface oxide thickness due to work hardening under PWR conditions [28, 29].

EDS point analyses were conducted in order to determine the chemical composition of the double layered oxide for a crack tip extending into the bulk metal, see Fig. 10A. The EDS spectra of the oxide film at the crack tip are consistent with the external surface oxide, and are presented in Fig. 10B. The inner oxide has been verified as a de-alloyed Ni-depleted chromium-iron based oxide, while the outer oxide is solely iron enriched. This is in agreement with the respective inner and outer oxide studies on stainless steels under PWR conditions [5,30]. Furthermore, Fig. 10A as well as Figs. 11 and 12 confirm that the outer oxide is typically more continuous at the surface and near the crack flanks while the inner oxide is of a fine-grained porous nature at the crack tip. Based on these results, it can be considered that the inner oxide is the resultant of Cr-selective diffusion-corrosion while the outer oxide is redeposited in retrospect of the matrix corrosion processes. The latter is supported by the non-homogenous outer oxide precipitates along the crack flanks and external surfaces.

From a detailed analysis of oxide diffraction patterns illustrated in Figs. 11C and 12C respectively, it is concluded that the most probable structure matching the experimental data for the inner oxide is $FeCr_2O_4$, also referred to as chromite (see also supplementary data). The lattice constant of the fcc-type spinel oxide is 0.8365 nm [31]. Still, the small traces of Si found in the EDS spectra suggest that the main oxide is not completely homogeneous, but rather that silicates may inherently substitute within the inner oxide. The presence of Si in the inner oxide is not totally surprising due to the high Si content of the substrate matrix. Strained silicate bonds are typically prone to rupture under aqueous environments, as has been suggested by silicate fracturing models [32]. This implies that Si has a generally adverse effect to the SCC resistance of this type of model alloy. On the other hand, the outer oxide is characterized as the fcc-type $(Fe,Ni)_3O_4$ with a lattice parameter of 0.8338 nm [33] due to strong iron-rich EDS signal with small substitute traces of Ni (see supplementary information for the simulated SAED diffraction pattern and a list of crystal family spacings). The structure complies as a plausible candidate for the outer oxide considering that the iron-nickel ratio may vary between 2.6Fe-0.4Ni to Fe2-Ni without reasonable change in the lattice structure. The true Ni-content of the outer oxide may be estimated from representative EDS spectra.
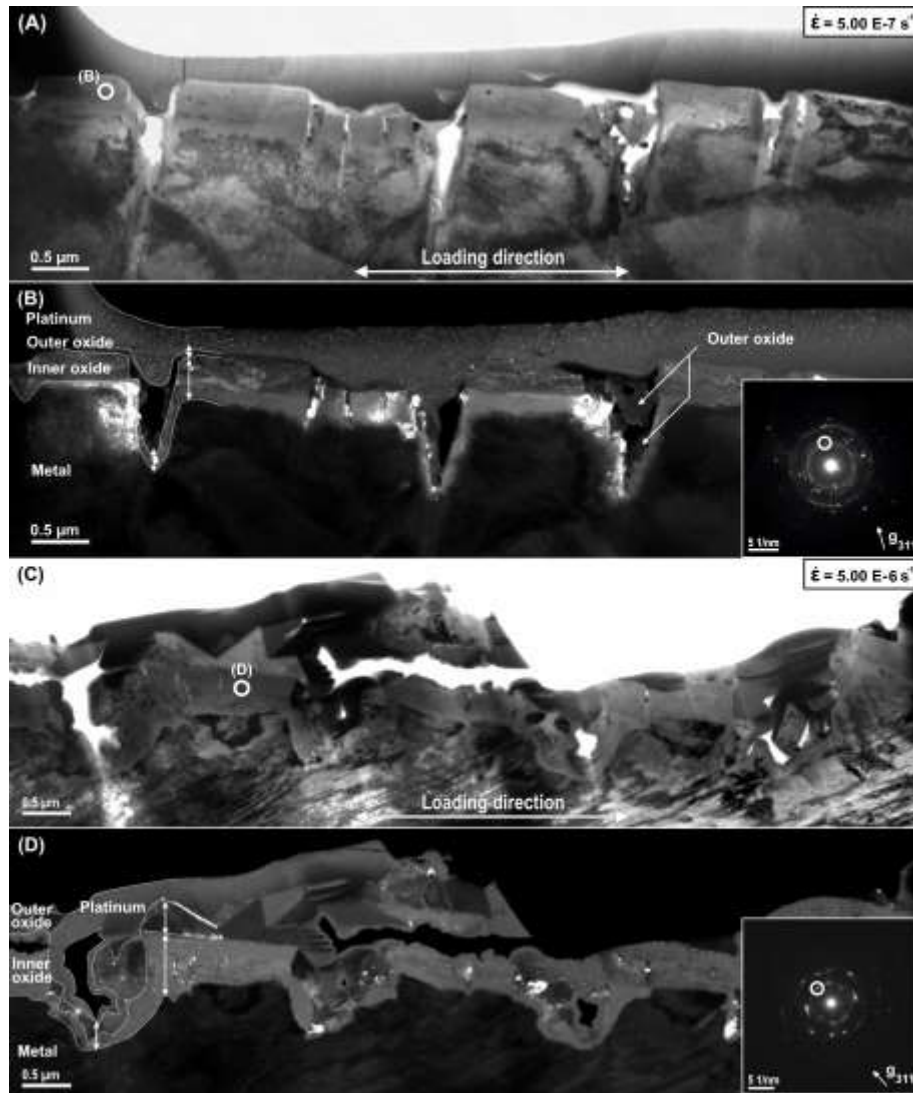
Fig. 8: Corresponding BF- and centralized DF-TEM appertaining to specimens strained to A-B: $\dot{\epsilon}$ = 5.00 E-7 s^{-1}, and C-D: $\dot{\epsilon}$ = 5.00 E-6 s^{-1}. The inset diffraction patterns correspond to the SAED locations shown as white circles in the respective BF-TEM micrographs. Indications of the different phases are representative of the thickness measurements presented in Fig. 9. The objective aperture centering is displayed and the indexing corresponds to the verified main oxide component FeCr$_2$O$_4$ (see also Fig. 11).
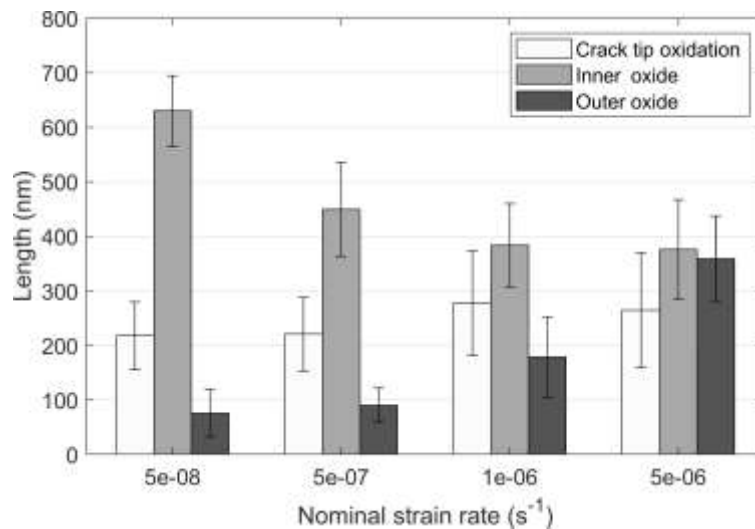

Fig. 9: External and crack tip oxide thickness measurements obtained from the BF- and centralized DF-TEM images for the varying strain-rates.
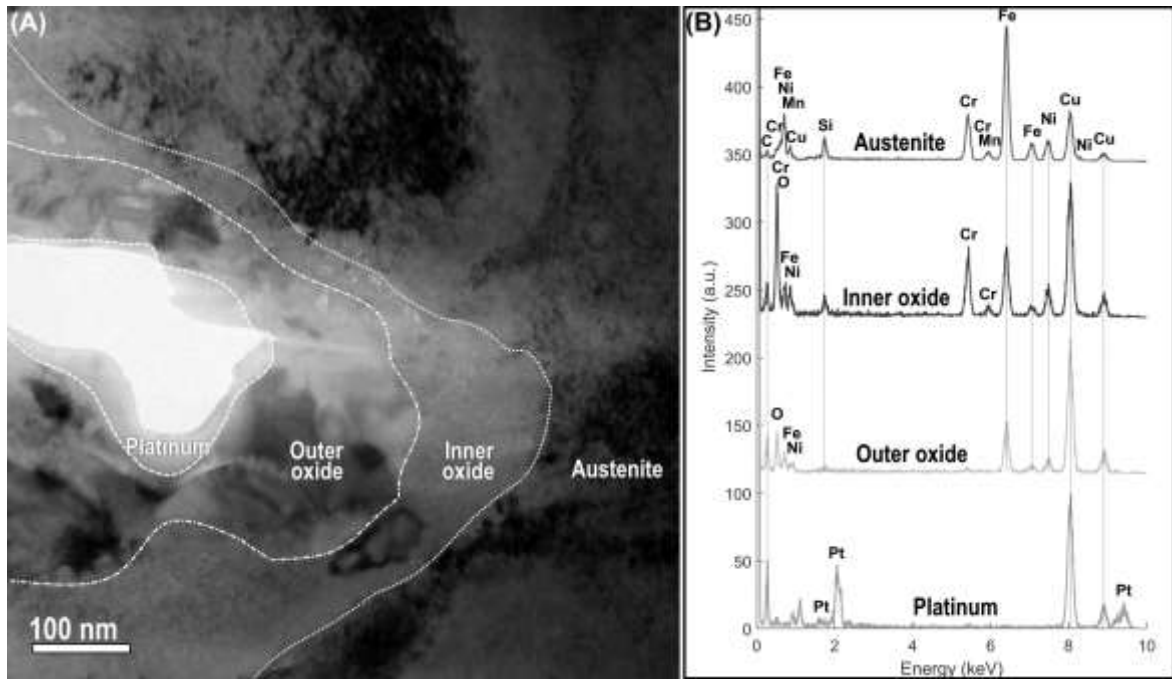
Fig. 10: A: BF-TEM SCC crack from a specimen strained to $\dot{\varepsilon}$ = 5.00 E-7 s^{-1}. B: Corresponding EDS spectra of different features surrounding the crack tip. The Cu signal originates from the cupper TEM support grid.
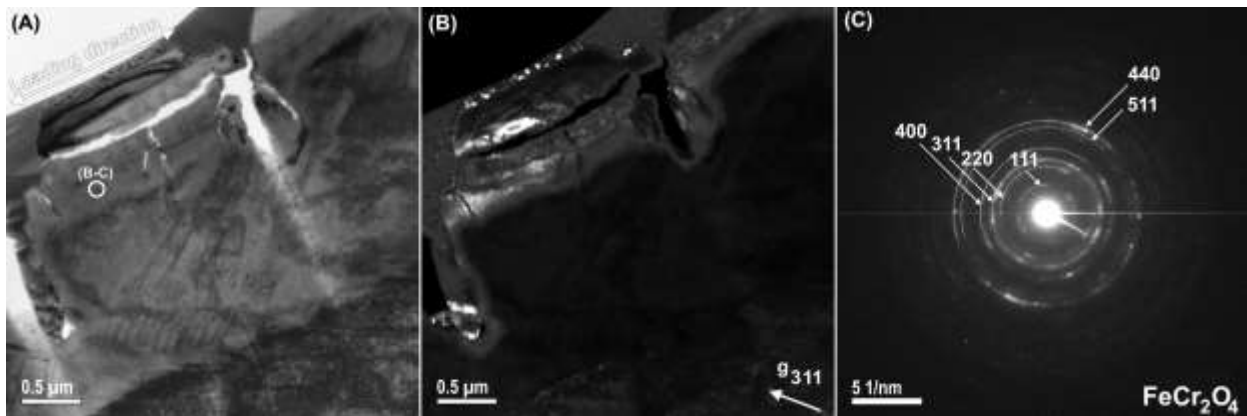

Fig. 11: Inner oxide for a specimen strained to $\dot{\varepsilon}$ = 1.00 E-6 s^{-1}. A-B: Corresponding BF- and centralized DF-TEM of the inner oxide in between two crack tips, with C: the corresponding indexed inner oxide diffraction pattern for $FeCr_2O_4$.
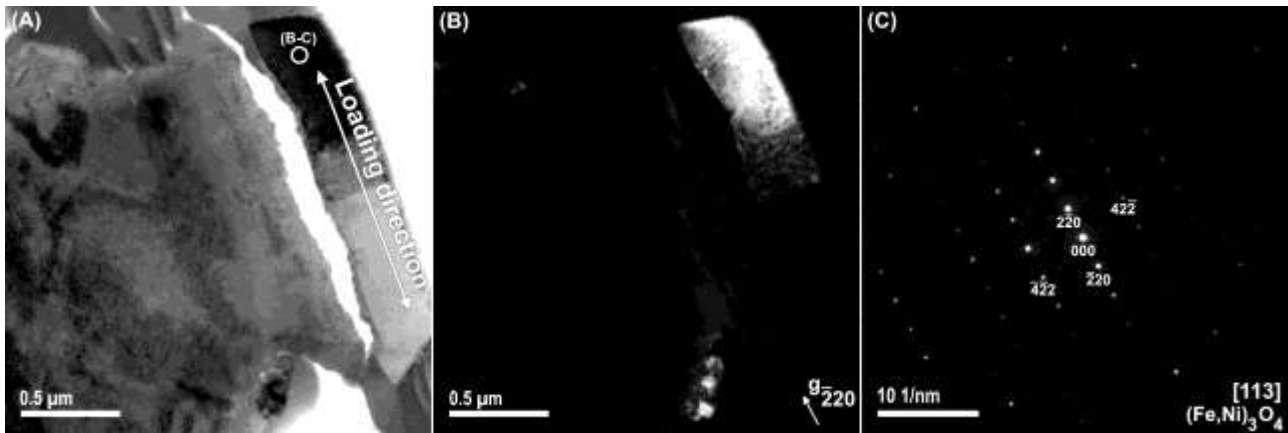
Fig. 12: $(Fe,Ni)_3O_4$ debonded outer oxide for a specimen strained to $\dot{\epsilon}$ = 1.00 E-6 s^{-1}. A-B: Corresponding BF and centralized DF-TEM of an outer oxide grain in between two crack tips, with C: the corresponding [113] diffraction pattern. The outer oxide is loosely connected due to a brittle fracture occurring at the interface with the inner oxide.

3.3 SCC mechanisms

In all SCC mechanism of stainless steel operating in PWR temperature water, oxidation plays a detrimental role. Therefore, it is expected that the information on crack morphology, and in particular the crack tip oxidation, should help to elucidate the dominant stress corrosion cracking mechanism. Since re-oxidation may occur after the initial crack is formed, it is of crucial importance to deduce under which conditions the oxide kinetics govern the crack initiation and propagation. In contrast to stainless steels at ambient temperature where oxide films have thicknesses in the nm range [34], PWR temperature oxide layers are up to several microns thick.

One renowned SCC mechanism is based on slip-dissolution [2,35] where a sufficient thick oxide film at the crack tip is required for oxide film rupture to occur. A second example is the internal oxidation model [2,36] where oxidation of the grain boundary at the crack tip is imperative as oxide cracking alone is responsible for the crack initiation and propagation. These two examples typically lead to intergranular fracture surfaces. However, for transgranular SCC in PWR temperature water, there is no consensus on which model best describes the observed phenomena. The presence of strong deformation fields in close vicinity of the crack tips indicates that one needs to consider an interplay of both corrosion- and deformation-driven cracking mechanisms. In our observations, different sample exposure times occurring at different strain-rates play a role in favor of one mechanism over the other. On the one hand, at long exposure times with slow strain-rates up to $\dot{\epsilon}$ = 5.00 E-7 s^{-1}, a diffusion-based oxidation process precedes the crack formation. However, for shorter exposure times at faster strain-rates starting from $\dot{\epsilon}$ = 1.00 E-6 s^{-1} and onwards, intrinsic failure is not as much dominated by corrosion but rather induced by the high external deformation rates. Respectively, the observed dominant SCC failure mechanisms depending on the strain-rate have been linked to the film-induced cleavage and strain-induced failure mechanisms.

The film-induced cleavage (FIC) model is presented as a respectable candidate that requires a material covered with a sufficiently thick surface layer that is sensitive to brittle fracture. Thus far, the FIC model [25,26,37,38] has not been

applied to transgranular SCC in PWR temperature water, though it applies well to experimental results observed for SCC cracks in stainless steels at low strain-rates for long exposure times. Accordingly, it is required that a sufficiently thick nanoporous film develops as a result of anodic diffusion-dissolution processes, that is susceptible to brittle fracture. These prerequisites for the FIC are typical for stainless steels in PWR environments and are supported by our findings. Internal microcleavage cracking within the porous layer may occur on the account of several actors, primarily being the externally applied surface stress. The FIC mechanism postulates that small successive cleavage cracks are introduced, much alike the sharp crack illustrated in Fig. 6, in the de-alloyed (nickel-depleted) oxide film. After propagation, surface re-oxidation of the exhausted crack tip occurs while in contact with the primary water. Evidence of Ni-enrichment ahead of the crack tips [5], which has been reported for stainless steels in high-temperature water, may be the resultant of this de-alloying process. The FIC can potentially induce transgranular crack growth under PWR conditions, and has already been linked to the SCC failure of stainless steels in other corrosive environments [38,39].

On the other hand, for shorter exposure times at faster strain-rates, SCC cracks propagating within the brittle oxide at increased growth rates typically show an increase in crack tip roughness [41,42]. Rounded shaped crack tips can be related to the strain-induced dislocation slipping in the surrounding microstructure under the influence of the high external deformation rates. Strain-induced crack tip failure is hence associated with the dislocation dynamics and stress-strain profiles in the near vicinity of the crack tips [5]. As the straining ensues, the localized deformation becomes more severe and additional microstructural defects such as twin systems are introduced. Primary mechanical twins initiate along favorable austenitic crystallographic <111> directions in the early stages of deformation. Secondary twinning systems may become activated under the increased degree of deformation, deeper within the bulk specimen, although this was less observed in the present work. Twin-slip interactions are known to induce strain hardening as the dislocation slip is inhibited due to the increase in twin interfaces [43,44]. This process is commonly understood as the dynamical Hall-Petch effect [45]. The strain-hardening increase from a microscopical perspective strongly associates with the mechanical failure data of fast-strained tapered specimens which has been reported in previous work [19].

One could refer to the use of transmission kikuchi diffraction (TKD) in further studies regarding SCC crack initiation, especially while focusing on the strain distribution in the vicinity of the crack tip through lattice misorientation mapping. This could affirm the deformation-based failure mechanism associated with our observations of SCC at high strain-rates. Additionally, scanning transmission electron microscopy (STEM) imaging and elemental mapping using high-angle annular dark-field (HAADF) and/or electron energy-loss spectroscopy (EELS) SI may refine the characterization of various phases in addition to what has been presented in this work.

4   Conclusions

The objective of the present study is to gain new insights on the SCC mechanism in CERT-strained high Si stainless steel tapered specimens exposed to a simulated PWR environment by FIB and TEM analyses of SCC crack-tips. Microstructural analyses based on crack morphology investigations support two distinct nominal strain-rate

dependent failure regimes. Slow strain-rate crack tips up to $10^{-6}\,s^{-1}$ demonstrate a narrow cleavage type appearance which could best be associated with the film-induced cleavage model, while faster strain-rates beyond $10^{-6}\,s^{-1}$ exemplify SCC cracks governed by a strain-induced failure. Twinning is reported as the main deformation pathway under increased forms of tensile stress. The brittle oxidation film is duplex by nature, with a confirmed $FeCr_2O_4$ inner and $(Fe,Ni)_3O_4$ outer fcc spinel type oxides.

Acknowledgements

References

1. P. L. Andresen, "Emerging issues and fundamental processes in environmental cracking in hot water (Reprinted from Proceedings of the CORROSION/2007 research topical symposium "Advances in Environmentally Assisted Cracking", 2007)," Corrosion, vol. 64, no. 5, pp. 439–464, 2008.
2. S. Lozano-Perez, J. Dohr, M. Meisnar, and K. Kruska, "SCC in PWRs: Learning from a Bottom-Up Approach," Metallurgical and Materials Transactions E, vol. 1, no. 2, pp. 194–210, 2014.
3. K. Arioka, T. Yamada, T. Miyamoto, and M. Aoki, "Intergranular stress corrosion cracking growth behavior of Ni-Cr-Fe alloys in pressurized water reactor primary water," Corrosion, vol. 70, no. 7, pp. 695–707, 2014.
4. T. Terachi, T. Yamada, T. Miyamoto, and K. Arioka, "SCC growth behaviors of austenitic stainless steels in simulated PWR primary water," Journal of Nuclear Materials, vol. 426, no. 1-3, pp. 59–70, 2012.
5. X. Liu, W. Hwang, J. Park, D. Van, Y. Chang, S. H. Lee, S. Y. Kim, S. Han, and B. Lee, "Toward the multiscale nature of stress corrosion cracking," Nuclear Engineering and Technology, vol. 50, no. 1, pp. 1–17, 2018.
6. Was, G. S. and Andresen, P. L. (2020). Mechanisms behind irradiation assisted stress corrosion cracking. In S. Ritter (Ed.). Nuclear corrosion: research, progress and challenges (pp. 47-88), EFC Publications No. 69, Woodhead Publishing, ISBN: 978-0-12-823719-9
7. P. Scott, "2000 F.N. speller award lecture: Stress corrosion cracking in pressurized water reactors interpretation, modeling, and remedies," Corrosion, vol. 56, 08 2000.
8. G. S. Was and P. L. Andresen, "Stress corrosion cracking behavior of alloys in aggressive nuclear reactor core environments," Corrosion, vol. 63, no. 1, pp. 19–45, 2007.
9. O. K. Chopra and A. S. Rao, "A review of irradiation effects on LWR core internal materials - IASCC susceptibility and crack growth rates of austenitic stainless steels," Journal of Nuclear Materials, vol. 409, no. 3, pp. 235–256, 2011.
10. S. M. Bruemmer, E. P. Simonen, P. M. Scott, P. L. Andresen, G. S. Was, and J. L. Nelson, "Radiation-induced material changes and susceptibility to intergranular failure of light-water-reactor core internals," Journal of Nuclear Materials, vol. 274, no. 3, pp. 299–314, 1999.
11. G. S. Was, Y. Ashida, and P. L. Andresen, "Irradiation-assisted stress corrosion cracking," Corrosion Reviews, vol. 29, no. 1-2, pp. 7–49, 2011.
12. R. W. Bosch, M. Vankeerberghen, R. Gérard, and F. Somville, "Crack initiation testing of thimble tube material under PWR conditions to determine a stress threshold for IASCC," Journal of Nuclear Materials, vol. 461, pp. 112–121, 2015.
13. R. W. Bosch, S. Ritter, M. Herbst, R. Kilian, M. G. Burke, J. Duff, F. Scenini, Y. Gu, A. Dinu, U. Ehrnstén, A. Toivonen, R. Novotny, O. Martin, F. J. Perosanz, A. Legat, and B. Zajec, "Stress corrosion crack initiation testing with tapered specimens in high-temperature water–results of a collaborative research project," Corrosion Engineering Science and Technology, vol. 0, no. 0, pp. 1–16, 2020.
14. J. Bai, S. Ritter, H. P. Seifert, and S. Virtanen, "Using tapered specimens to study the effect of hydrogen and surface finish on SCC initiation in Alloy 182 under boiling water reactor conditions," Corrosion Engineering Science and Technology, vol. 52, no. 8, pp. 558–566, 2017.
15. J. Bai, S. Ritter, H. P. Seifert, M. Vankeerberghen, and R. W. Bosch, "The use of tapered specimens to evaluate the SCC initiation susceptibility in alloy 182 in BWR and PWR environments," Minerals, Metals and Materials Series, pp. 1929–1948, 2019.

16. R. N. Singh, R. Lala Mikin, G. K. Dey, D. N. Sah, I. S. Batra, and P. Ståhle, "Influence of temperature on threshold stress for reorientation of hydrides and residual stress variation across thickness of Zr-2.5Nb alloy pressure tube," Journal of Nuclear Materials, vol. 359, no. 3, pp. 208–219, 2006.

17. J. Yu, L. J. Xue, Z. J. Zhao, G. X. Chi, and R. N. Parkins, "Determination of Stress Corrosion Crack Initiation Stress and Crack Velocities Using Slowly Strained Tapered Specimens," Fatigue & Fracture of Engineering Materials & Structures, vol. 12, no. 6, pp. 481–493, 1989.

18. R. Kilian, S. Berger, R. Bosch, S. Ritter, U. Ehrnsten, F. Perosanz, A. Hojna, K. Nikbin, O. Martin, R. Novotny, A. Dinu, G. Burke, B. Zajec, and A. Legat, "D16.4.2 Draft NUGENIA Proposal for optimized surface conditions to mitigate in-service degradation (NUGENIA Position Paper)," pp. 1–31, 2016.

19. A. Penders, M. J. Konstantinović, R. Bosch, and D. Schryvers, "Crack initiation in tapered high si stainless steel specimens – stress threshold analyses," Corrosion Engineering, Science and Technology, vol. 55, no. 8, pp. 721–728, 2020.

20. R. Kilian and B. Devrient, "Experimental data on crack initiation, fp6 project perfect deliverable c35c," tech. rep., VTT, SCK CEN, EdF, Uni Manchester, NAMRC, Wood, Framatome, CVR, 2008.

21. I. D. Curieres, "Corrosion in PWR Stainless Steel Components : a TSO perspective based on Operating Experience and Expertises," in FONTEVRAUD 8, vol. 46, 2014.

22. S. Lozano-Perez, "A guide on FIB preparation of samples containing stress corrosion crack tips for TEM and atomprobe analysis," Micron, vol. 39, no. 3, pp. 320–328, 2008.

23. T. Ishitani, K. Umemura, T. Ohnishi, T. Yaguchi, and T. Kamino, "Improvements in performance of focused ion beam cross-sectioning: Aspects of ion-sample interaction," Journal of Electron Microscopy, vol. 53, no. 5, pp. 443–449, 2004.

24. T. H. Loeber, B. Laegel, S. Wolff, S. Schuff, F. Balle, T. Beck, D. Eifler, J. H. Fitschen, and G. Steidl, "Reducing curtaining effects in FIB/SEM applications by a goniometer stage and an image processing method," Journal of Vacuum Science & Technology B, Nanotechnology and Microelectronics: Materials, Processing, Measurement, and Phenomena, vol. 35, no. 6, p. 06GK01, 2017.

25. K. Sieradzki, R. C. Newman, and R. C. Newman, "Brittle behavior of ductile metals during stress-corrosion cracking," Philosophical Magazine A: Physics of Condensed Matter, Structure, Defects and Mechanical Properties, vol. 51, no. 1, pp. 95–132, 1985.

26. R.C. Newman, K. Sieradzki (1987) Film-Induced Cleavage During Stress-Corrosion Cracking of Ductile Metals and Alloys. In: Latanision R.M., Jones R.H. (eds) Chemistry and Physics of Fracture. NATO ASI Series (Series E: Applied Sciences), vol 130. Springer, Dordrecht.

27. R.E. Ricker, J.L. Fink, E. Escalante, Evidence of film-induced cleavage by electrodeposited Rh, Corros. Deform. Interact. (1993) 733–740.

28. S. Lozano-Perez, K. Kruska, I. Iyengar, T. Terachi, and T. Yamada, "The role of cold work and applied stress on surface oxidation of 304 stainless steel," Corrosion Science, vol. 56, pp. 78–85, 2012.

29. K. Kruska, S. Lozano-Perez, D. W. Saxey, T. Terachi, T. Yamada, and G. D. Smith, "3D atom-probe characterization of stress and cold-work in stress corrosion cracking of 304 stainless steel," 15th International Conference on Environmental Degradation of Materials in Nuclear Power Systems-Water Reactors 2011, vol. 2, pp. 891–898, 2011.

30. K. Kruska, S. Lozano-perez, D. W. Saxey, T. Terachi, T. Yamada, and G. D. W. Smith, "Nanoscale characterisation of grain boundary oxidation in cold-worked stainless steels," Corrosion Science, vol. 63, pp. 225–233, 2012.

31. D. Lenaz, H. Skogby, F. Princivalle, and U. Hålenius, "Structural changes and valence states in the MgCr2O4FeCr2O4 solid solution series," Physics and Chemistry of Minerals, vol. 31, no. 9, pp. 633–642, 2004.

32. T.A. Michalske, S.W. Freiman, A Molecular Mechanism for Stress Corrosion in Vitreous Silica, J. Am. Ceram. Soc. 66 (1983) 284–288.

33. K.N. Subramanyam, Neutron and X-ray diffraction studies of certain doped nickel ferrites, J. Phys. C Solid State Phys. 4 (1971) 2266–2268.

34. D. Ramachandran, R. Egoavil, A. Crabbe, T. Hauffman, A. Abakumov, J. Verbeeck, I. Vandendael, H. Terryn, D. Schryvers, TEM and AES investigations of the natural surface nano-oxide layer of an AISI 316L stainless steel microfibre, J. Microsc. 264 (2016) 207–214.

35. F.P. Ford, P.L. Andresen, Corrosion in nuclear systems: environmentally assisted cracking in light water reactors, in: P. Marcus (Ed.), Corrosion Mechanisms in Theory and Practice, Marcel Dekker, Inc., 2002, pp. 605–642.

36. P.M. Scott and M. Le Calvar: in Proceedings of the Sixth International Symposium on Environmental Degradation of Materials in Nuclear Power Systems—Water Reactors, 1993, pp. 657–65.

37. Turnbull, "Modelling of Environment Assisted Cracking," Corrosion Science, vol. 34, no. 6, pp. 921–960, 1993.

38. R. E. Ricker, J. Fink, and E. Escalante, "Evidence of film-induced cleavage by electrodeposited Rh," Corrosion Deformations Interactions, no. January 1993, pp. 733–740, 1993.

39. R.C. Newman, R.R. Corderman, K. Sieradzki, Evidence for dealloying of austenitic stainless steels in simulated stress corrosion crack environments, Br. Corros. J. 24 (1989) 143–148.

40. W.J. Nisbet, G.W. Lorimer, R.C. Newman, A transmission electron microscopy study of stress corrosion cracking in stainless steels, Corros. Sci. 35 (1993) 457–469.

41. M. J. Buehler and H. Gao, "Dynamical fracture instabilities due to local hyperelasticity at crack tips," vol. 439, no. January, pp. 307–310, 2006.

42. M. J. Buehler, F. F. Abraham, and H. Gao, "Hyperelasticity governs dynamic fracture at a critical length scale," pp. 141–146, 2003.

43. I. Karaman, H. Sehitoglu, Y. Chumlyakov, and H. Maier, "The deformation of low-stacking-fault-energy austenitic steels," JOM, vol. 54, pp. 31–37, July 2002.

44. H. Idrissi, K. Renard, D. Schryvers, and P. J. Jacques, "On the relationship between the twin internal structure and the work-hardening rate of TWIP steels," Scripta Materialia, vol. 63, no. 10, pp. 961–964, 2010.

45. A. Butz, M. Zapara, A. Erhart, D. Croizet, N. Sten, J. Hagstrom, D. Helm, M. Schneider, M. Kampczyk, A. Haufe, M. Biasutti, D. Gmbh, S. K. Ab, S. Mannesmann, F. Gmbh, and F. A. Gmbh, "Plenary Sessions Deformation Behavior of Twip-Steels : From Experiments To Constitutive Modelling and Simulations," no. June, pp. 38–48, 2014.